ELSEVIER

Contents lists available at ScienceDirect

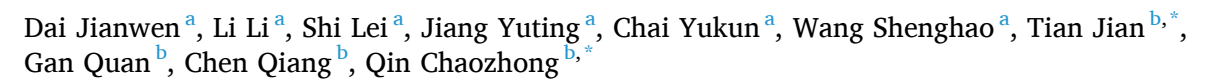
Journal of Hydrology

journal homepage: www.elsevier.com/locate/jhydrol



Research papers

Limiting pathways and breakthrough pressure for CO₂ flow in mudstones



- ^a Shenzhen Branch of China National Offshore Oil Corporation, Shenzhen 518054, China
- ^b State Key Laboratory of Coal Mine Disaster Dynamics and Control, Chongqing University, Chongqing 400044, China

ARTICLE INFO

This manuscript was handled by Huaming Guo, Editor-in-Chief, with the assistance of Mingjie Chen, Associate Editor

Keywords: Breakthrough pressure Multiscale porous structures Pore-network modeling Mudstones

ABSTRACT

The sealing and integrity of caprocks is a critical issue in the geological sequestration of CO₂. In this work, we integrate multiscale pore-size measurements and imaging techniques, to characterize macropores, microporosity, and their spatial connectivity of intact mudstone cores from an Enping oilfield in the South China Sea. Together with the information on mineral compositions, we propose clay regions in the absence of organic matter as limiting pathways for supercritical CO₂ flows in the cores, which primarily consist of nanopores ranging from tens to hundred nm in diameter. The FIB-SEM tomography is used to obtain nanoporous structures of a representative domain of those limiting pathways. We simulate the primary drainage of supercritical CO₂ displacing brine in the domain by using an in-house quasi-static pore-network model. The numerical predictions of capillary breakthrough pressure match the experimental data well. Our proposed method of determining capillary breakthrough pressure can substantially complement experimental measurements. Moreover, it has the potential to quantitatively link the multiscale porous structures of mudstone to its CO₂ sealing.

1. Introduction

CO₂ emission induced by human activities is the main cause of global climate change. The IPCC report pointed out that to control the global temperature rise within the established 1.5 °C range at the end of this century, the world must rapidly reduce carbon emission to 25 gigatons of CO2 equivalent by 2030 and negative carbon emissions of more than 10 gigatons per year after 2050 (IPCC, 2018). To tackle the global climate challenge, the China government has made a solemn commitment to achieve carbon peak by 2030 and carbon neutrality by 2060 (The Central People's Government of the People's Republic of China). CO₂ geological sequestration is currently the most effective method for reducing carbon emissions (Jiang et al., 2019; Sun et al., 2020; Kumar et al., 2018; Wang et al., 2023). The sealing and integrity of caprocks are essential for the feasibility and safety of CO₂ geological sequestration. Research on CO₂ geological sequestration mainly involves CO₂-water--rock reactions, mechanical failure under cyclic injections, and capillary breakthrough pressure (Elkhoury Jean et al., 2015; Jayasekara et al., 2020; Lyu et al., 2023; Zhang et al., 2020, 2023). Among these, the breakthrough pressure of caprocks directly affects the reservoir pressure control and the maximum plume height of sequestration during CO2 injection, which is one of the most important parameters to assess the ${
m CO}_2$ sequestration capacity (Li et al., 2022; Espinoza and Santamarina, 2017)

As one of the most common types of caprock, mudstone has formed very low porosity and permeability during the long process of compaction, diagenesis, and later geological evolution, to allow them to play an important role in the sequestration and accumulation of oil and gas (Guo et al., 2022; Liu et al., 2015; Zhao et al., 2020). With the intensification of the greenhouse effect, mudstone has been studied as an important potential caprock for the geological sequestration of CO₂. For instance, Hou et al. investigated the geological sequestration capacity of mudstones from the Da'anzhai formation in Sichuan Basin, China for CO2 by using petrological analysis and numerical simulations. The results showed that the reaction of key minerals such as calcite, dolomite, and kaolinite after CO₂ injection resulted in self-sequestration for CO₂ (Hou et al., 2022). Zhang et al. studied on CO₂ sequestration capacity of the Upper mudstone caprock of the No.3 Coal Seam in Qinshui Basin, China (Zhang et al., 2021). Then, they found that the super-critical CO₂water-rock reaction caused the formation of dissolved pores, resulting in macroscopically increased pore volume and permeability of the reservoir. At the same time, the formation of some secondary mineral precipitates may block the CO2 flow channel to some extent. Therefore, the CO₂ sequestration capacity of mudstone caprock will decrease in the

E-mail addresses: tianjian2171@cqu.edu.cn (T. Jian), chaozhong.qin@cqu.edu.cn (Q. Chaozhong).

^{*} Corresponding authors.

early stage and increase slightly in the late stage. Hence, it is suggested to select the strata with good reservoir integrity and undeveloped fissure as the object of CO_2 sequestration. Jayasekara et~al. studied the effect of super-critical CO_2 -saline-rock interaction on the sequestration capacity of overlying CO_2 in the South-west Hub geo-sequestration project mudstone caprock effect, and they believe that the risk of the mineral reaction to the safety of CO_2 sequestration by mudstone caprock mainly depends on the change of the net pore volume of mudstone after the mineral reaction (Jayasekara et al., 2020). However, the contents of these key reactive minerals in mudstone caprock tend to be extremely low, geological sequestration of CO_2 still relies on the compacted structure of mudstone. Therefore, given wettability and interfacial tension conditions, studying the capillary breakthrough pressure of mudstone caprock itself become the main purpose of analyzing the CO_2 geological sequestration capacity of mudstone caprock.

Since the breakthrough pressure of caprock cannot be directly obtained by field test, the CO2 sequestration capacity of caprock has been measured via core flow experiments (Wu et al., 2020). In virtue of facile procedure and good data accessibility, the mercury intrusion test is the most widely used method for breakthrough pressure estimation (Hildenbrand et al., 2002; Egermann et al., 2006; Pittman, 1992; Dewhurst et al., 2002; Heath et al., 2012). Nevertheless, the major limitation of the assessment of breakthrough pressure by mercury intrusion test is that the gas-mercury flow systems used in mercury intrusion tests cannot reflect the gas-water system in practical reservoirs, resulting in uncertainty in breakthrough pressure assessment. Hence, the gas-water twophase displacement experiment was usually used to obtain the breakthrough pressure of CO₂ flow inside the core (Kawaura et al., 2013; Rezaevan et al., 2015; Busch and Müller, 2011). However, the direct use of core displacement experiments on low-permeability rock such as mudstone has shortcomings such as long measurement time, high cost, and low repeatability (Busch and Amann-Hildenbrand, 2013). Therefore, a novel method for assessment of the breakthrough pressure of compacted rock is urgently needed.

Mudstone is a medium with multi-scale (nano-pores to micro-pores) pore structure, the clay minerals filled between the skeleton particles constitute the complex nano-pore flow area of mudstone, which is an important reason for the low porosity and permeability of mudstone (Li et al., 2021). For this reason, the key to studying the CO₂ breakthrough pressure of mudstone is to reveal the control effect of such nano-pore flow zone on CO2 flow capacity. Using scanning electron microscope (SEM) and mercury intrusion technology (MICP), Li et al. characterized the shallow mudstone reservoir in Zhanhua Sag in East China Capillary breakthrough pressure and CO2 sequestration capacity. They believe that the content of clay minerals is the most important factor controlling the sequestration capacity of mudstone in this zone (Li et al., 2022). However, the specific correlation between clay minerals and CO₂ sequestration capacity of mudstone is not elucidated. Guiltinan et al. found that the breakthrough pressure of mudstone is also closely related to the composition of mudstone minerals and pore structure (Guiltinan et al., 2018). Unfortunately, they do not discuss the controlling effect of the nano/microporous zone formed by clay minerals on mudstone permeability, the flow behaviors and breakthrough pressure of CO2 flow in mudstones have rarely been linked to the clay minerals either.

In this study, by combining XRD, high-pressure Mercury Intrusion Porosimetry (MIP), SEM, and micro/nano CT scanning, the limiting pathways of CO_2 breakthrough in multi-scale pore structures of mudstones were defined. Then, an image-based pore network of a clay microporosity zone forming limiting pathways was constructed by using the FIB-SEM and image analysis techniques. By using our in-house quasistatic pore-network model, the seepage processes of CO_2 breakthrough were simulated, and the resultant capillary pressure curves were obtained. Furthermore, the effects of wettability on CO_2 seepage and breakthrough pressure were investigated. The limiting pathways and breakthrough pressure of CO_2 were evaluated from the perspective of mudstone multi-scale pore structures. It sheds light on the linkage

between porous structures and CO_2 breakthrough pressure. In addition, this study helped to improve the accuracy of indirect breakthrough pressure acquisition through mercury intrusion test, and effectively complement the existing breakthrough pressure evaluation techniques.

2. Materials and methods

The fluid flow behavior and phase permeability through rocks can be directly controlled by the pore structure and minerals composition of the rocks (Tan et al., 2023). Therefore, before we study the breakthrough pressure of CO2 flow in mudstone, its pore structure and minerals composition will be investigated. From Enping Oilfield in the South China Sea, we drilled samples at the underground depths of 991 m, 1201 m, and 1671 m to investigate the multiscale pore structures of mudstone caprocks, labeled as MS-1, MS-2 and MS-3, respectively. Then, the three mudstone samples were prepared into standard samples to carry out the XRD analysis, low-temperature N₂ adsorption test, micro/nano CT scanning, and FIB-SEM scanning to analyze their minerals composition and pore structures. After that, the pore structure of the clay microporosity pores was reconstructed to perform the CO₂ flow analysis. The whole procedure of our work was described in Fig. 1.

2.1. Rock mineral analysis

In order to analyze the components of the mudstone samples, XRD was used to conduct the rock mineral analysis. The Rigaku Ultima IV XRD was used to determine the contents of rock minerals in the three samples. First, the prepared sample was crushed into 1 mm particles for whole-rock mineral composition analysis. Then, the wet grinding method was employed to extract the clay minerals suspension, separated the clay particles by centrifuge, and added water to stir. Finally, the final obtained sample was spread on the ground glass sheet, and the clay composition determination was executed after natural air drying.

SEM was employed to further identify the mineral types and distributions. To achieve this goal, the backscattered electron probe equipped with the Helios 5 CX instrument was used to observe the pore types and distributions of mudstone. Due to the low strength of the mudstone samples themselves, they are easy to be broken and damaged. Therefore, the samples were cut into 8 mm \times 8 mm \times 3 mm blocks by means of wire cutting, and the samples were wrapped with epoxy resin when preparing the samples for electron microscopy observation. After the gummed samples were formed, mechanical polishing and argon ion polishing were performed on the front and back of the observation surface to ensure that the observation surface could reach nanoscale flatness.

2.2. Multi-scale pore structure analysis

In this study, low-temperature N_2 adsorption experiment and high-pressure mercury intrusion test were combined to analyze the mudstone pore size distribution, so as to reveal characteristics of multiscale pore structures of mudstone. Additionally, micro-CT and FIB-SEM were used to analyze pore structures and connectivity of clay microporosity zones, and macro porous zone of mudstone. Among them, we focused on the control effect of the clay microporosity zone on the overall seepage pathway of mudstone and provided a real digital core for the subsequent pore-scale simulations of super-critical CO_2 flow.

2.2.1. Low-temperature N_2 adsorption test

The low-temperature N_2 adsorption experiment was performed to characterize the distribution of the nanoscale pores of mudstone. First, the mudstone was grand to pieces and sifted through a 60 \sim 80 mesh sieve to collect about 5 g samples. Then, the selected samples were subjected to vacuum extraction and heat pretreatment. After that, the ASAP2460 automatic gas adsorption instrument was used for the adsorption experiment and obtained related parameters of nano-pores in mudstone by using adsorption amounts under different balanced

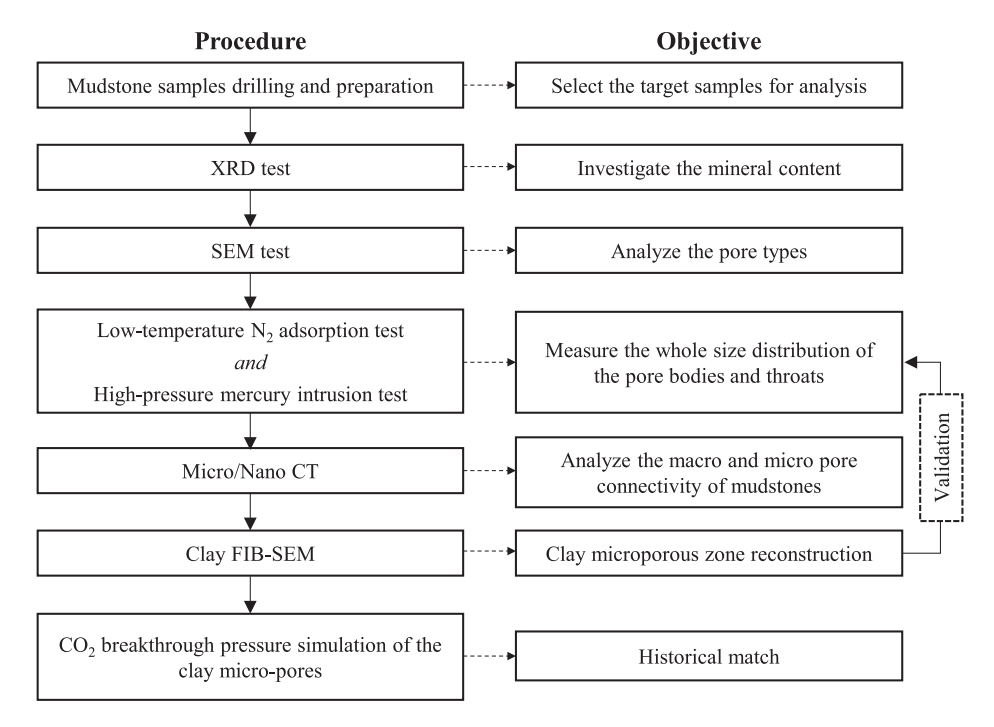


Fig. 1. Schematic flowcharts of the CO2 breakthrough pressure investigation of this work.

relative pressure points.

2.2.2. High-pressure mercury intrusion test

Mudstone develops with multi-scale pores, and low-temperature N_2 adsorption can only analyze the nanoscale pores. To measure the pore size distribution of multi-scale pores of mudstone, a high-pressure mercury intrusion experiment was carried out. About 2 \sim 3 g bulk sample of the mudstone was prepared to perform the high-pressure mercury intrusion experiment. After drying at a low-temperature environment, the AutoPoreIV9500 device was used for a high-pressure mercury intrusion test. The maximum mercury intrusion pressure could reach 200 MPa with a relative pore size ranging from 5 nm to 800 μm during the test. The mercury pressure was gradually increased (up to 200 MPa) to overcome the capillary force and invade the pore of the sample. Finally, pore structure characteristics such as pore size distribution were determined according to the amount of mercury input under different pressures.

2.2.3. Characterization by micro/nano CT and FIB-SEM

To analyze the multi-scale pore connectivity of mudstone, the sample was first scanned using the GE Phoenix Nanoom S to reconstruct the macroporous pore regions of the mudstone with a resolution of 1 μm . Then, the Helios 5 CX was used for 3D imaging under focused ion beam scanning electron microscopy (SEM), with a resolution of 10 nm and slice spacing of 20 nm for the reconstruction of clay 3D microporosity structures.

2.3. Quasi-static pore-network model

Our in-house quasi-static pore-network model is used to simulate ${\rm CO_2}$ flow in the mudstones. First, an open-source extraction code, PoreSpy, has been used to obtain the pore-network connectivity and geometric information of individual pores (Gostick, 2017). Watershed segmentation is used in the construction of pore bodies, while pore throats connecting pore bodies are volumeless. The used quasi-static pore-network code considers key two-phase displacement mechanisms such as cooperative filling of pore bodies, piston-type move, and snapoff. In addition, the cross-section of both idealized pore and throat

elements is represented by three different shapes, namely circle, square, and triangle. This classification is based on Morrow's 'shape factor', $G = A/P^2$, where A is the cross-sectional area, and P is the perimeter. The shape factor for triangles, square, and circles are $0 \sim \sqrt{3/36}$, $\sqrt{3/36} \sim 1/16$ and more than 1/16, respectively (Mason and Morrow, 1991). For the irregulated triangle and the square pore-throat element, we consider the effects of wetting phase residual in the corner to saturation, displacement type, and conductivity. For more details, one can refer to Qin's published work (Qin et al., 2021).

3. Results and discussion

3.1. Multi-scale pore structures of mudstone

The mineral composition of mudstone caprocks has an obvious controlling effect on their CO_2 sequestration performance. Therefore, the mineral composition of the mudstone samples used in this study was investigated. Based on the XRD analysis, the minerals component of the mudstone samples with different depths is similar, as shown in Table 1. It analyzed that the main mineral component of mudstone samples in our case is quartz (content = $53\% \sim 77\%$) followed by clay (content = $16\% \sim 33\%$). Besides, potash feldspar, plagioclase, dolomite, calcite, and pyrite all exist in small amounts in these mudstone samples (content = $7\% \sim 14\%$). As observed, it suggested that the formation depth could have a certain effect on the contents of the mineral components in mudstone caprocks. With the increase of depth, the content of quartz in mudstones gradually increases. At the same time, the content of clay in mudstones gradually decreased, and the main composition of clay changed from illite to illite/smectite mixture as shown in Table 2.

To analyze the pore structure of the mudstone caprocks, the 2D SEM analysis of the mudstone samples was performed first. As shown in Fig. 2, the intergranular pores were the main pore types of the mudstone samples. However, the spaces of these intergranular pores were almost filled by many microporosity pores contributed from the clay minerals (Fig. 2-b, d, f), resulting in the formation of a multi-scale pore structure in mudstones. Additionally, it contains a very small number of organic matter pores (Fig. 2-a, only found in sample MS-1), further contributing to the nano-scale pore structure of the mudstone caprocks. Owing to the

Table 1
Results of the mineral composition of the mudstone samples used in this study.

Sample ID	Permeability, mD	Depth, m	Mass fraction (%)							
			quartz Q	potash feldspar Kfs	plagioclase Ab	dolomite Dol	calcite Cal	pyrite Py	total Clays	
MS-1	1.61×10^{-3}	991	53.6	1.5	6.7	2.8	2.2	0.6	32.6	
MS-2	$8.64 imes 10^{-3}$	1201	65.4	6.4	3.8	0.0	2.0	0.9	21.4	
MS-3	4.93×10^{-3}	1671	76.3	3.8	2.1	0.0	0.4	0.9	16.5	

Table 2
Results of the clay minerals component of the mudstone samples used in this study.

Sample ID	Depth, m	Mass fraction smectite S	(%) illite/smectite mixture I/S	illite It	kaolinite Kao	chlorite Chl	Mixing ratio (%) I/S
MS-1 MS-2	991 1201	-	29 40	38 25	18 22	15 13	50 50
MS-3	1671	_	50	22	18	10	50

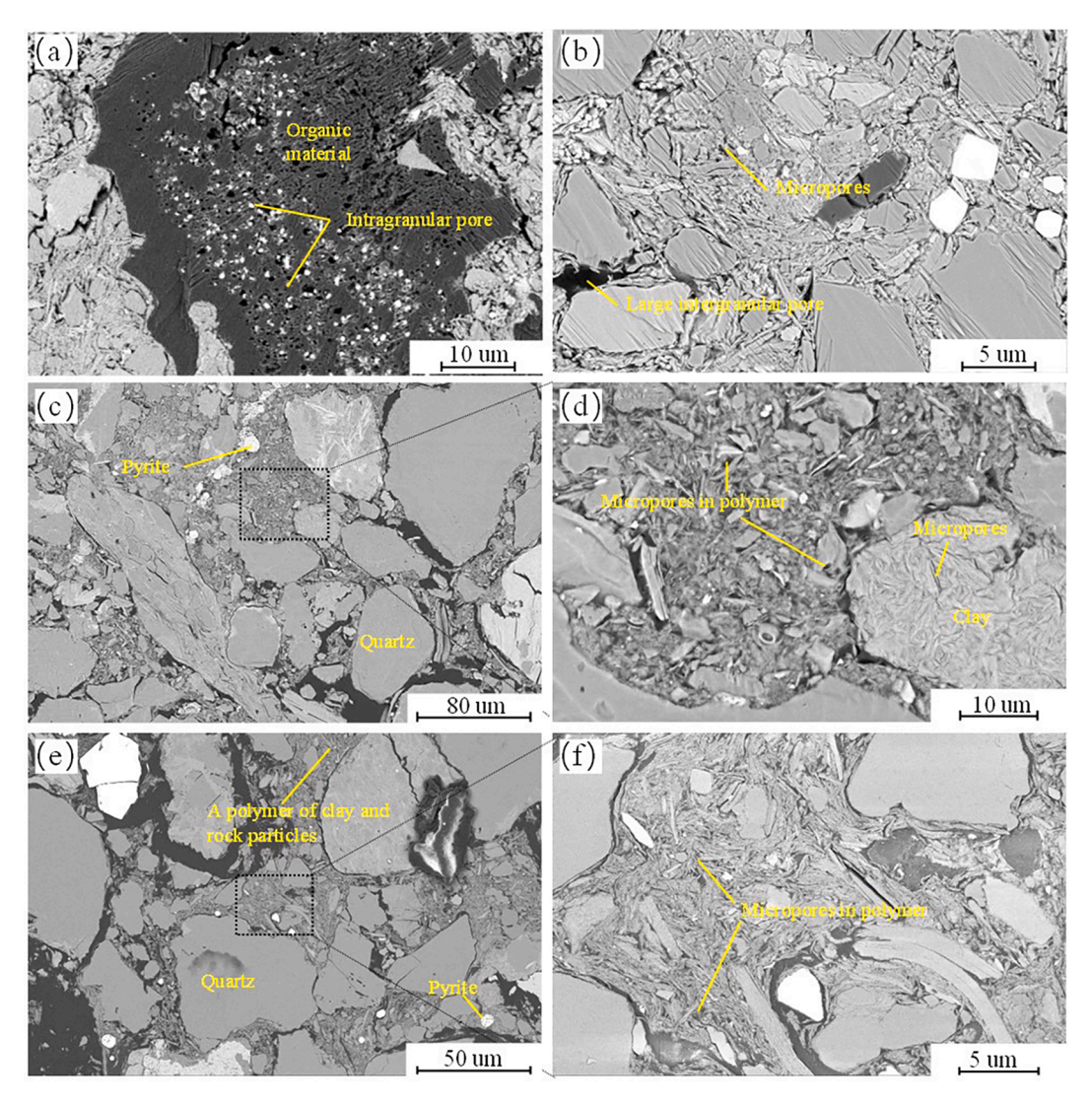


Fig. 2. SEM results of the mudstone samples in this study. (a) Electron microscopic image of organic matter mineral in sample MS-1; (b) Clay cement and its internal pore structure in sample MS-1; (c) The mineral distribution in sample MS-2, 60% of the mineral is quartz, the spaces between quartz are filled with clay and other cement; (d) The clay structure in sample MS-2; (e) The mineral distribution of sample MS-3 (similar to sample MS-2); (f) The clay structure in sample MS-3.

filling of clay minerals, the mudstone caprocks form their low porosity and low permeability nature. Because the content of the organic matter was too small, its influence on the pore structure and permeability of mudstone caprocks was neglectful. Thus, it can be inferred that the pore spaces were filled by clay minerals to form a remarkable microporosity pores region, which is the key factor to limit the flow pathways and

breakthrough pressure of CO₂ in mudstone caprocks.

In order to quantitatively analyze the multi-scale pore structure of mudstone caprocks, the pore sizes of the mudstone samples were investigated. Firstly, the mudstone samples were used to perform the low-temperature N2 adsorption experiment to characterize the distribution of the nano-scale pores. As observed in Fig. 3, the adsorption-desorption curve shape of the three samples is approximately consistent. When $P/P_0 > 0.45$, the desorption curve was above the adsorption curve for all the mudstone samples. According to the BET formula, the pore size of these samples at the corresponding pressure at the time of curves convergence is mainly in the range of 3 nm, which means that the adsorption isotherm hysteresis loop effect and the loop of the curve forced shutdown phenomenon occurs in this pore size range (Brunauer et al., 1938). On the other hand, combined with the classification of the adsorption loop recommended by the International Union of Pure and Applied Chemistry (IUPAC) (Thommes et al., 2015), the adsorption loop curves of all mudstone samples are similar to the loop curves H3 type. Basically, the adsorption and desorption curves of the three samples have no obvious inflection points, indicating that the morphology of the nanoscale pore in the experimental sample is mainly slit flat and has good connectivity.

According to Fig. 4, the pore sizes distribution of three mudstone samples drilled from different formations is similar, with the pore size mainly distributed in the range of 2 \sim 10 nm and the average peak appearing at 2.7 nm, which is consistent with the pore size range corresponding to the forced closure phenomenon in the adsorption–desorption curve. Combined with the above SEM observation analysis, we can see that samples contained a small amount of organic matter, indicating that the 3 nm pore size peak of the $\rm N_2$ adsorption test may be mainly derived from the contribution of organic matter. Therefore, to clarify the microporous zone pore size range of mudstone composed of clay minerals, it is necessary to further analyze mudstone pore size and connectivity.

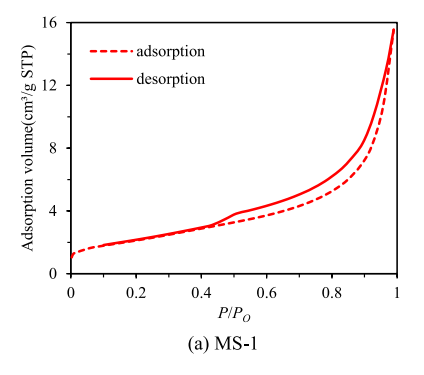
The low-temperature N2 adsorption experiment mainly characterized the pore throat distribution of pore size range 2 \sim 60 nm, and the peak value of pore size is suspected to mainly contain the contribution of organic matter. To further analyze the distribution range of microporosity pores and macro pores in mudstone, a high-pressure mercury intrusion test was carried out. Because the sample MS-2 was broken during the experiment, the analysis was carried out based on the results of MS-1 and MS-3. Fig. 5 indicates that there is a clear multi-scale pore structure from nanometer to micron in both samples, of which the microporosity pores size peak mainly appears in $10 \sim 100$ nm, and the average peak value is 60 nm (MS-1) and 20 nm (MS-3), respectively. Moreover, combined with SEM images and N2 adsorption results, we can further conclude that the macro-pores of mudstone caprocks are mainly composed of intergranular pores with an average pore size of about 8 μm, the microporosity zone of mudstone is composed of clay pores below 100 nm, and a very small amount of organic matter with pores less than 10 nm. Given that the content of organic matter is minimal, its impact on mudstone permeability and CO_2 flow can be ignored. Therefore, we give the hypothesis that the microporosity zones of clay minerals in the mudstone are the key pore structures controlling the CO_2 flow behavior and capillary breakthrough pressure in mudstone caprocks. Then, the hypothesis will be demonstrated later.

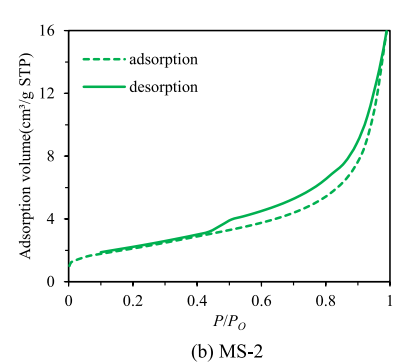
3.2. Pore connectivity of mudstone

Low-temperature N₂ adsorption and high-pressure mercury intrusion tests show that the mudstone samples used in this study have significant multi-scale pore size distributions with the coexistence of macro porous and microporosity regions. Especially, the microporosity region is mainly dominated by those pores in the range of 10 nm to 100 nm. To evaluate the effects of the microporosity region on the CO₂ flow pathways and breakthrough pressure in the mudstone caprocks, it requires further study of the pore connectivity between the microporosity region and the macro pores. Here, based on the above pore structure analysis, 1 μm was selected as the spatial resolution of scanning to conduct 3D CT scanning on MS-1, MS-2, and MS-3 to analyze the connectivity between macro pores and microporosity pores in mudstone. AVIZO was used to carry out the segmentation of CT images to obtain the microporosity zone, macro porous zone, as well as the spatial distribution and percentages of the matrix of the samples, and the results were summarized in Table 3. From the 3D imaging of the macro pores, it can be found that the connectivity of the sample is poor, and there is an obvious layering phenomenon. On the other hand, the microporosity pores are filled between the large pores to connect, which matches the analysis results of electron microscopy scanning, suggesting that to maintain the connection structure between the macro porous zones, the microporosity zone is required as a bridging medium. As a result, these widely distributed microporosity zones in mudstone connected in series with the macro porous region form the connected flow channel of mudstone. This analysis suggests the existence of microporosity zones that limit the flow path and breakthrough pressure of CO₂ in mudstone. Based on the results, the pore size peak of the macro porous zones matches the peak of the pore size distribution around 7 µm in the high-pressure mercury intrusion results, seen in Fig. 6, proving that our analysis is reliable.

3.3. Porous structures of limiting pathways

For the samples involved in this study, it can be concluded that clay pores with pore sizes range of $10 \sim 100$ nm are the limiting pathways controlling the CO_2 breakthrough pressure of mudstone. In this section, MS-1 was used as a representative sample to investigate the pore connectivity between the macro porous and microporosity regions. At first, a multisite scanning of MS-1 using FIB-SEM was performed and a representative clay minerals zone that did not contain organic matter was selected from the results for cutting and scanning analysis. Then, the scanned 1042 SEM images were imported into AVIZO software, and use the automatic calibration module to correct the images, and then use





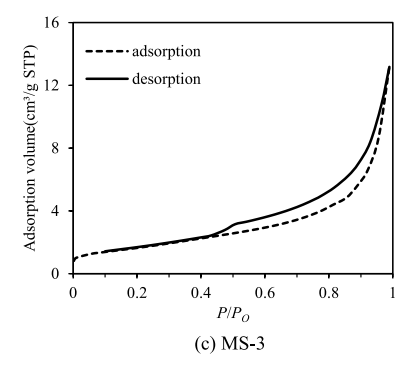


Fig. 3. Adsorption-desorption curves of mudstone samples.

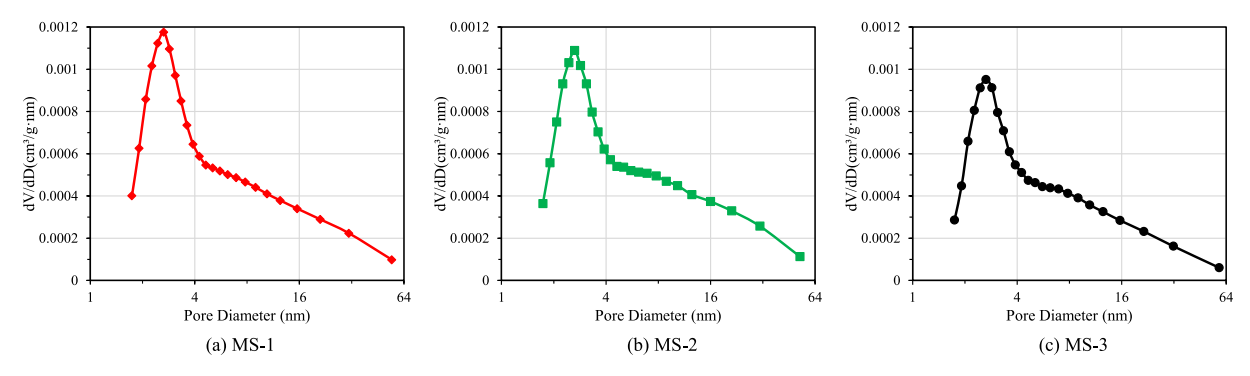


Fig. 4. Pore size distribution of mudstone samples under low-temperature N2 adsorption.

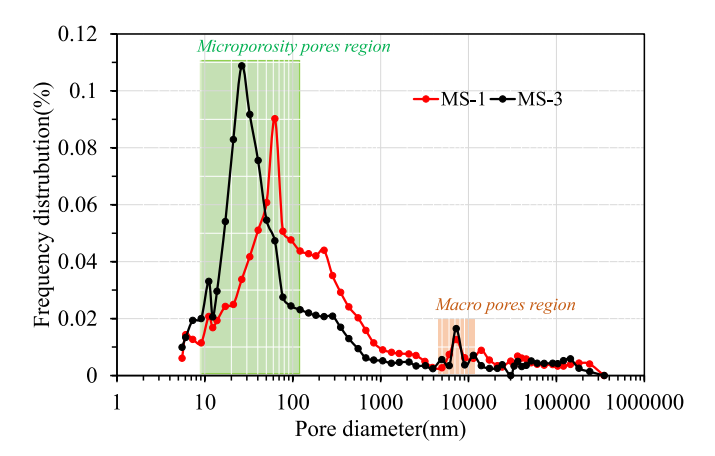
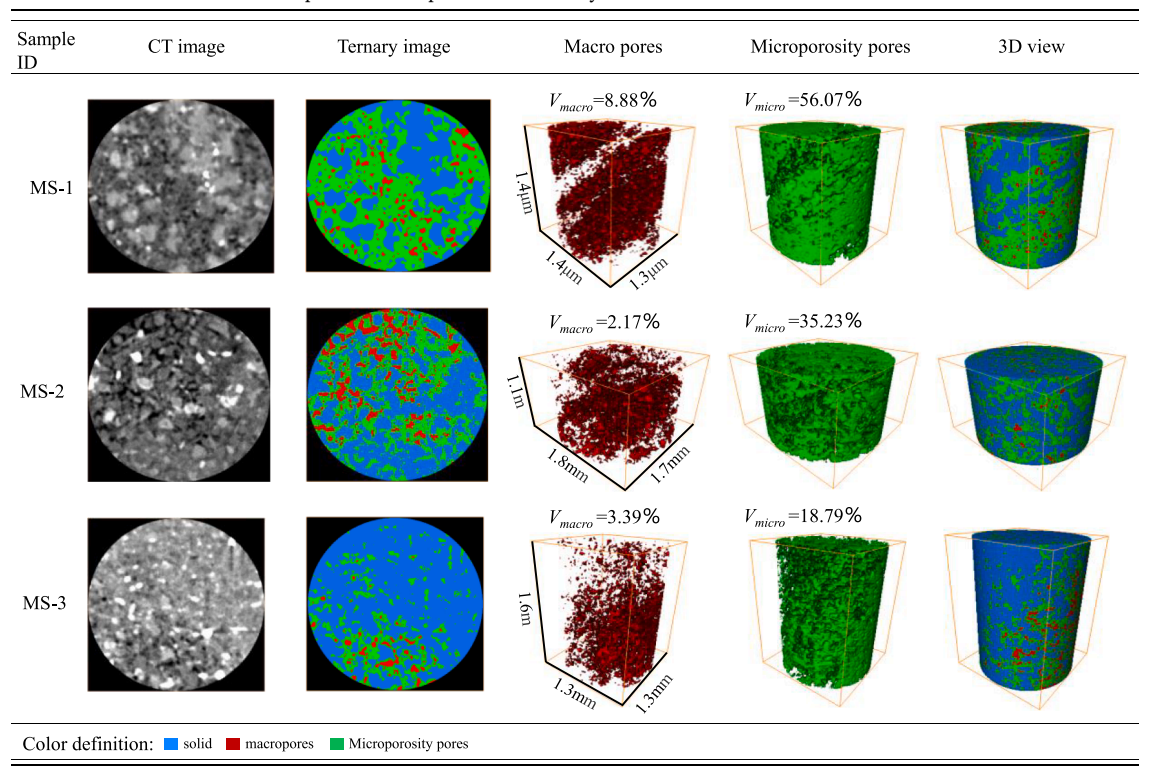


Fig. 5. Pore size distributions of mudstone samples obtained by high-pressure mercury intrusion test.

non-local means Filter to eliminate noise and curtain effect. To improve the calculation efficiency and eliminate the influence of large rock particles on the results, we selected the clay minerals-rich region with a real size of $10 \times 10 \times 10$ µm from the preprocessed image as the object of study. After resizing the voxel resolution to be10 nm, the actual size of the entire image was $1000 \times 1000 \times 1000$. The final 3D scan grayscale image of the clay zone is shown in Fig. 7 (a). Fig. 7 (b) shows the nanoporous structure obtained after threshold segmentation. According to Fig. 7 (b), the nano-pores in the clay zone are of slit type with a wide size distribution, and the larger pores are mainly developed at the junction between the clay and the larger mineral particles, while the pores inside the clay are relatively small. Finally, the SNOW algorithm is used to extract the mudstone pore network using PoreSpy, and the pore network in the clay minerals is shown in Fig. 7 (c).

Fig. 8 shows the diameter distribution of the tangential circle of the pore throat and the pore network coordination distribution of the microporosity region pore network model. It can be found from the figure that the main pore size distribution range is between 10 nm and 100 nm with the peak value of nano-pore diameter distribution is about 45 nm, which matches with the high-pressure mercury intrusion data.

Table 3Statistical results of mudstone samples micro-CT pore structure analysis.



(b)

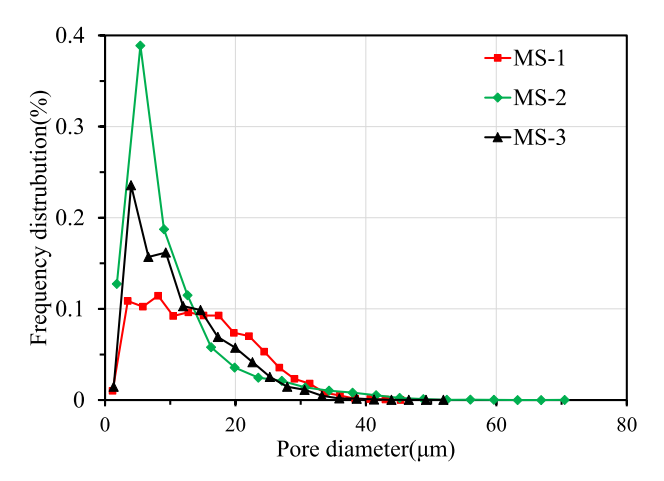


Fig. 6. Pore size distributions of the macro porous zones of mudstone samples obtained by CT scanning images analysis.

The average coordination number of the pore network is around 3.57 after excluding those isolated pores, which indirectly confirms that the microporous zones have good pore connectivity so that they can play the role of a bridge connecting the macroporous zones in the mudstone samples.

3.4. Breakthrough pressure of supercritical CO2

The previous work claimed that it can cause CO₂-clay minerals geochemical reactions during a long-time CO₂ injection scenario, which in

turn changes the pore structure of the mudstones and the caprock integrity (Jayasekara et al., 2020). In our present study, we are interested in the presence of clay microporosity pores on the whole pore connectivity of the mudstone, and investigating their effects on the CO2 flow pathways and breakthrough pressure in a short-time scale, the geochemical reactions are not our current concern. To investigate the CO2 flow behavior and estimate its breakthrough pressure at reservoir stress conditions, the throat diameter of the established model of the microporosity pores in clay was transformed to suit the effective stress effect. The conversion formula of the throat size was described as follow (Song et al., 2020):

$$r = r_0 \left(\frac{1 - \left(\frac{\sigma_{eff}}{p_1}\right)^m}{1 - \left(\frac{\sigma_{eff0}}{p_1}\right)^m} \right)^{\frac{2}{3}}$$
 (1)

where r refers to the corrected pore radius under effective stress effect, r_0 is the origin pore radius obtained from the FIB-SEM analysis, σ_{eff} is the actual effective stress exerted to the clay nano-pores under the reservoir's stress condition, and the effective stress of sample M−1 is around 10 MPa in our case, σ_{eff0} is the experimental effective stress exerted to the clay nano-pores during the FIB-SEM scanning, p_1 is the effective stress of clay nano-pores when they are completely closed, and the value is 100 MPa, *m* is the roughness coefficient of the pore surface (0.675 in this case). By transforming the crustal stress parameter, the throat diameter in the model was transformed, wherein the transformed pore size ranges from 10 nm to 80 nm, with a peak of about 35 nm. Therefore, in the actual simulation, the transformed pore size was employed for

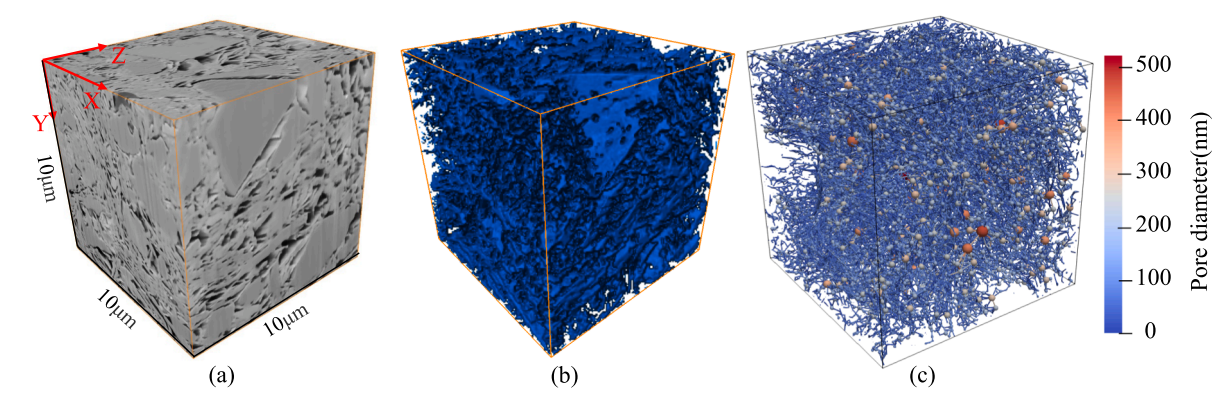


Fig. 7. Cropped study area from the original FIB-SEM image (a), threshold segmentation of the extracted clay area 3D pore structure (b), and the clay area pore network model extracted using SNOW algorithm (c).

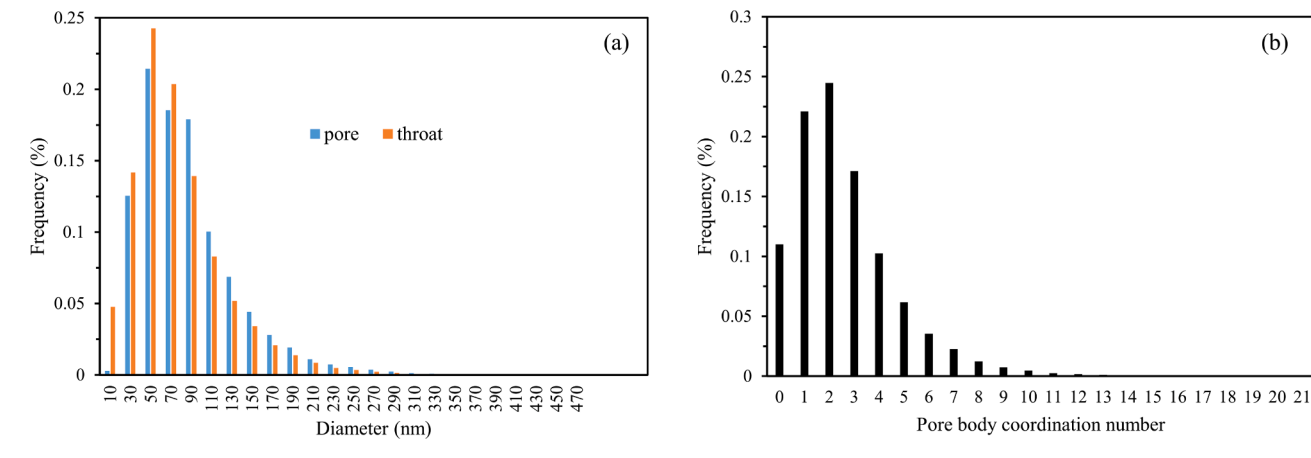


Fig. 8. Pore and throat diameter distribution (a) versus frequency of coordination (b).

simulation calculation. The CO₂ seepage and breakthrough pressure process were numerically simulated under two wetting conditions, respectively. They are homogeneous wettability environments with a contact angle of 35° and heterogeneous wettability with a contact angle evenly distributed from 25° to 50° environments. This is largely due to two reasons: 1) to keep our case study falling into the hydrophilic conditions; and 2) to compare the influence of heterogeneous and uniform wettability on CO₂ transport. The experimental results are shown in Fig. 9. As observed, a breakthrough was observed in a homogeneous wettability environment when the overall CO2 saturation of the microporous zone of mudstone reached 0.29; in a heterogeneous wettability environment, the overall CO2 saturation of the microporous zone of mudstone at CO2 breakthrough was 0.36, indicating that the seepage relationship between CO2 and water in the microporous zone of mudstone is more complex, the CO₂ seepage ability is relatively more limited, and the breakthrough saturation is higher. The CO₂ breakthrough saturation at the microporous zone scale studied in this study differs from the CO₂ breakthrough saturation at the core scale due to the different scales, where the CO2 breakthrough saturation is determined by the proportion of connected channels consisting of macropores and the microporous zone.

According to capillary pressure curves (Fig. 10), the pressure of CO₂ breakthrough calculated in the two wettability environment simulations was 1.87 MPa and 1.89 MPa, respectively, with no significant difference. According to the Young-Laplace equation (Li et al., 2005), the minimum throat diameter in the microporous zone for CO2 breakthrough was calculated to be about 70 nm. In conjunction with the results of the mineral component analysis of the mudstone samples presented in previous studies (Heath et al., 2012), we found that the samples in this study were consistent with the mudstone samples mineral component of the Lower Tuscaloosa Group in a previous study. In addition, when the contact angle of the 8 mudstone samples they tested was 37°, the estimated CO_2 breakthrough pressure range was $0.03\sim5.31$ MPa and the average breakthrough pressure was 3.14 MPa. Among them, the breakthrough pressure of the sample LT8590.9 was 1.87 MPa, which was consistent with the results of our analysis, which just confirmed the reliability of the proposed breakthrough pressure prediction method. The permeability of mudstone samples MS-1 was measured at 1.61×10^{-5} ³ mD before the experiment. It is slightly higher than permeability 0.63 \times 10⁻³ mD calculated for microporous zone formed by clay minerals only. This can be attributed to the fact that compared to microporosity

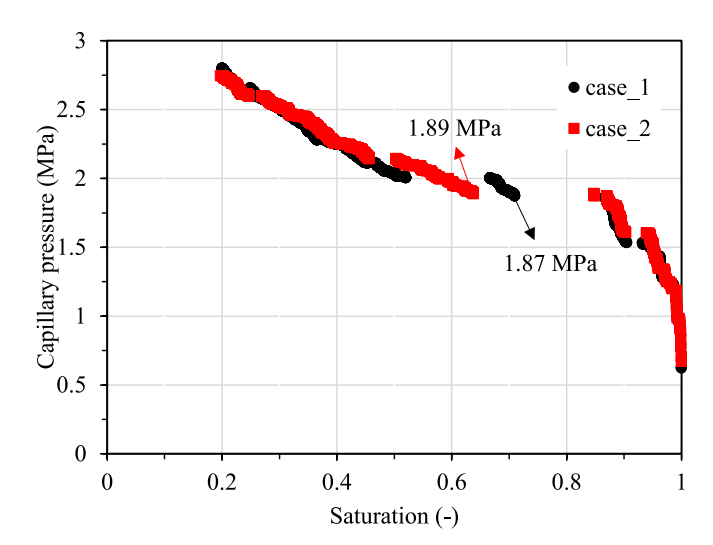


Fig. 10. Simulation results of capillary pressure curves for ${\rm CO_2}$ -water system based on microporous zone.

zones, the core scale contains more macroporous zones to increase the pore connectivity, resulting in a slightly higher overall permeability than the microporous zone only. In fact, the little difference between the microporous zone permeability and the core sample's overall permeability just further proved that the rock permeability and ${\rm CO_2}$ breakthrough pressure are essentially determined by the microporosity zone composed of clay minerals in the mudstone caprocks.

4. Conclusions

By integrating several multiscale pore-size measurements and imaging techniques such as SEM, micro CT, FIB-SEM, N_2 adsorption, and high-pressure MIP, we found that the mudstones have remarkable multiscale pore structures ranging from a few nanometers to tens of microns. The macropores in the sizes of microns are isolated, which are connected by the microporosity of clays at the core scale. By analyzing the connectivity of mudstone pore structures, we identified the limiting pathways for CO_2 breakthrough in the mudstones as the microporosity of clay minerals with main pore diameters of $10 \sim 100$ nm. The FIB-SEM

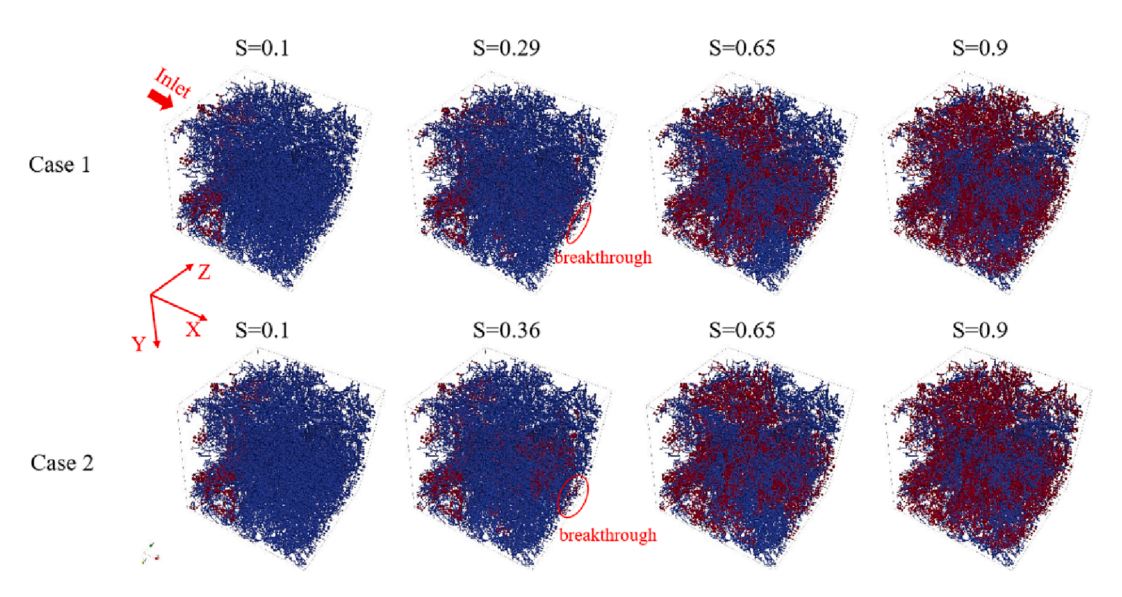


Fig. 9. Above: Simulation results of CO_2 flow and distribution in the microporous zone at a contact angle of 35°. Below: Simulation results of CO_2 flow and distribution in the microporous zone at a contact angle of 25 to 50° . Pores and throats that have been invaded by non-wetting phases are marked in red, while pores and throats occupied by wetting phases are marked in blue. (For interpretation of the references to colour in this figure legend, the reader is referred to the web version of this article.)

was employed for quantitative analysis and 3D reconstruction of the limiting pathways. The pore size distribution of the FIB-SEM digital core matches the mercury intrusion data well. The breakthrough pressure through the identified limiting pathways predicted by the pore network model is around 1.88 MPa. Based on the Young-Laplace equation, the corresponding breakthrough (or critical) pore diameter is around 70 nm. Our proposed method of determining capillary breakthrough pressure can substantially complement experimental measurements. Moreover, it has the potential to quantitatively link the multiscale porous structures of mudstone to its CO_2 sealing.

CRediT authorship contribution statement

Dai Jianwen: Methodology, Funding acquisition. Li Li: Funding acquisition. Shi Lei: Funding acquisition. Jiang Yuting: Funding acquisition. Chai Yukun: Validation, Funding acquisition. Wang Shenghao: Funding acquisition. Tian Jian: Methodology, Investigation, Data curation, Writing – original draft, Formal analysis, Funding acquisition. Gan Quan: Project administration, Funding acquisition. Chen Qiang: Supervision, Funding acquisition. Qin Chaozhong: Writing – review & editing, Supervision.

Declaration of Competing Interest

The authors declare that they have no known competing financial interests or personal relationships that could have appeared to influence the work reported in this paper.

Data availability

No data was used for the research described in the article.

Acknowledgements

The authors gratefully acknowledge the financial support of the Project of Technical Research and Application of CO_2 Capture and Storage in Enping Oilfield (No.YXKY-SXSH-2021-SZ-01), the National Natural Science Foundation of China (No. 52104024) and the China Postdoctoral Science Foundation (No. 2021M700606).

References

- Brunauer, S., Emmett, P.H., Teller, E., 1938. Adsorption of gases in multimolecular layers. J. Am. Chem. Soc. 60 (2), 309–319.
- Busch, A., Amann-Hildenbrand, A., 2013. Predicting capillarity of mudrocks. Mar. Pet. Geol. 45, 208–223.
- Busch, A., Müller, N., 2011. Determining CO₂/brine relative permeability and capillary threshold pressures for reservoir rocks and caprocks: recommendations for development of standard laboratory protocols. Energy Procedia 4, 6053–6060.
- Dewhurst, D.N., Jones, R.M., Raven, M.D., 2002. Microstructural and petrophysical characterization of Muderong Shale: application to top seal risking. Petrol. Geosci. 8 (4), 371–383.
- Egermann P, Lombard J M, and Bretonnier P. A Fast and Accurate Method to Measure Threshold Capillary Pressure of Caprocks under Representative Conditions, 2006, p. 46. SCA2006 A.
- Elkhoury Jean, E., Detwiler Russell, L., Pasha, A., 2015. Can a fractured caprock self-heal? Earth Planet. Sci. Lett. 417, 99–106.
- Espinoza, D.N., Santamarina, J.C., 2017. $\rm CO_2$ breakthrough—Caprock sealing efficiency and integrity for carbon geological storage. Int. J. Greenhouse Gas Control 66, 218–229.
- Gostick, J.T., 2017. Versatile and efficient pore network extraction method using marker-based watershed segmentation. Phys. Rev. E 96, 1–15.
- Guiltinan, E.J., Espinoza, D.N., Cockrell, L.P., Cardenas, M.B., 2018. Textural and compositional controls on mudrock breakthrough pressure and permeability. Adv. Water Resour. 121, 162–172.
- Guo, F., Xie, Z., Zhang, N., Zhang, C., Guo, H., Cui, G., Xiang, Z., 2022. Study on the Pore-throat structure characterization and nano grouting law of the Low-permeability mudstone based on NMR-RSM methods. Constr. Build. Mater. 342, 127913.
- Heath, J.E., Dewers, T.A., McPherson, B.J.O.L., Nemer, M.B., Kotula, P.G., 2012. Porelining phases and capillary breakthrough pressure of mudstone caprocks: Sealing efficiency of geologic CO₂ storage sites. Int. J. Greenhouse Gas Control 11, 204–220.
- Hildenbrand, A., Schlomer, S., Krooss, B.M., 2002. Gas breakthrough experiments on fine-grained sedimentary rocks. Geofluids 2 (1), 3–23.

- Hou, L., Yu, Z., Luo, X., Wu, S., 2022. Self-sealing of caprocks during CO₂ geological sequestration. Energy 252, 124064.
- Ipcc, 2018. Global warming of 1.5°C. An IPCC special report on the impacts of global warming of 1.5°C above pre-industrial levels and related global greenhouse gas emission pathways. In: The context of strengthening the global response to the threat of climate change, sustainable development, and efforts to eradicate poverty. World Meteorological Organization, Geneva, Switzerland.
- Jayasekara, D.W., Ranjith, P.G., Wanniarachchi, W.A.M., Rathnaweera, T.D., Chaudhuri, A., 2020. Effect of salinity on supercritical CO₂ permeability of caprock in deep saline aquifers: An experimental study. Energy 191, 116486.
- Jayasekara, D.W., Ranjith, P.G., Wanniarachchi, W.A.M., Rathnaweera, T.D., Van Gent, D., 2020. CO₂-brine-caprock interaction: Reactivity experiments on mudstone caprock of South-west Hub geo-sequestration project. J. Pet. Sci. Eng. 189, 107011.
- Jiang, L., Gonzalez-Diaz, A., Ling-Chin, J., Roskilly, A.P., Smallbone, A.J., 2019. Post-combustion CO₂ capture from a natural gas combined cycle power plant using activated carbon adsorption. Appl. Energy 245, 1–15.
- Kawaura, K., Akaku, K., Nakano, M., Ito, D., Takahashi, T., Kiriakehata, S., 2013. Examination of methods to measure capillary threshold pressures of pelitic rock samples. Energy Procedia 37, 5411–5418.
- Kumar, M., Sundaram, S., Gnansounou, E., Larroche, C., Thakur, I.S., 2018. Carbon dioxide capture, storage and production of biofuel and biomaterials by bacteria: a review. Bioresour. Technol. 247, 1059–1068.
- Li, S., Dong, M., Li, Z., Huang, S., Qing, H., Nickel, E., 2005. Gas breakthrough pressure for hydrocarbon reservoir seal rocks: implications for the security of long-term CO₂ storage in the Weyburn field. Geofluids 5 (4), 326–334.
- Li, Y.i., Lv, L., Ming, L., Yu, Q., 2022. Quantitative investigation of phase characteristic effects on CO₂ breakthrough pressures in unsaturated Low-Permeability sandstone. J. Hydrol. 609, 127780.
- Li, Y., Zha, M., Song, R., Aplin, A.C., Bowen, L., Wang, X., Zhang, Y., 2021. Microstructure and pore systems of shallow-buried fluvial mudstone caprocks in Zhanhua depression, east China inferred from SEM and MICP. Mar. Pet. Geol. 132, 105189.
- Li, C., Zhang, L., Luo, X., Zeng, Z., Xiu, J., Lei, Y., Cheng, M., Hu, C., Zhang, M., He, W., 2022. Clay mineral transformations of mesozoic mudstones in the central Junggar Basin, northwestern China: Implications for compaction properties and pore pressure responses. Mar. Pet. Geol. 144. 105847.
- Liu, W., Li, Y., Yang, C., Daemen, J.J.K., Yang, Y., Zhang, G., 2015. Permeability characteristics of mudstone cap rock and interlayers in bedded salt formations and tightness assessment for underground gas storage caverns. Eng. Geol. 193, 212–223.
- Lyu, X., Yun, L., Xu, J., Liu, H., Yu, X., Peng, P., Ouyang, M., Luo, Y.u., 2023. Sealing capacity evolution of gypsum salt caprocks under multi-cycle alternating stress during operations of underground gas storage. J. Pet. Sci. Eng. 220, 111244.
- Mason, G., Morrow, N.R., 1991. Capillary behavior of a perfectly wetting liquid in irregular triangular tubes. J. Colloid Interface Sci. 141, 262–274.
- Pittman, E.D., 1992. Relationship of porosity and permeability to various parameters derived from mercury injection-capillary pressure curves for sandstone. AAPG Bull. 76 (2), 191–198.
- Qin, C.-Z., van Brummelen, H., Hefny, M., Zhao, J., 2021. Image-based modeling of spontaneous imbibition in porous media by a dynamic pore network model. Adv. Water Resour. 152, 103932.
- Rezaeyan, A., Tabatabaei-Nejad, S.A., Khodapanah, E., et al., 2015. A laboratory study on capillary sealing efficiency of Iranian shale and anhydrite caprocks. Mar. Petrol. Geol. 66, 817–828.
- Song, W., Yao, J., Wang, D., Li, Y., Sun, H., Yang, Y., 2020. Dynamic pore network modelling of real gas transport in shale nanopore structure. J. Pet. Sci. Eng. 184, 106506.
- Sun, W., Shao, Y., Zhao, L., Wang, Q., 2020. Co-removal of CO₂ and particulate matter from industrial flue gas by connecting an ammonia scrubber and a granular bed filter. J. Clean. Prod. 257, 120511.
- Tan, Q., Kang, Y., You, L., Peng, H., Zhao, F., Bai, J., 2023. The role of salt dissolution on the evolution of petrophysical properties in saline-lacustrine carbonate reservoirs: Pore structure, porosity-permeability, and mechanics [J]. J. Hydrol. 618, 129257.
- The Central People's Government of the People's Republic of China. We aim to achieve carbon peak by 2030 and achieve carbon neutrality by 2060: Win the hard battle of low-carbon transition [EB/OL]. (2021-04-02) [2022-09-21]. http://www.gov.cn/xinwen/2021-04/02/content_5597403.htm.
- Thommes M, Kaneko K, Neimark A V, et al. Physisorption of gases, with special reference to the evaluation of surface area and pore size distribution (IUPAC Technical Report), Pure Appl. Chem, 2015, 87: 1051–1069.
- Wang, Z., Li, S., Jin, Z., Li, Z., Liu, Q., Zhang, K., 2023. Oil and gas pathway to net-zero: Review and outlook. Energ. Strat. Rev. 45, 101048.
- Wu, T., Pan, Z., Connell, L.D., Liu, B.o., Fu, X., Xue, Z., 2020. Gas breakthrough pressure of tight rocks: A review of experimental methods and data. J. Nat. Gas Sci. Eng. 81, 103408.
- Zhang, K.Q., Liu, L.R., Huang, G.H., 2020. Nanoconfined water effect on CO_2 utilization and geological storage. Geophys. Res. Lett. 47, e2020GL087999.
- Zhang, K., Sang, S., Zhou, X., Liu, C., Ma, M., Niu, Q., 2021. Influence of supercritical CO₂-H₂O-caprock interactions on the sealing capability of deep coal seam caprocks related to CO₂ geological storage: A case study of the silty mudstone caprock of coal seam no. 3 in the Qinshui Basin, China. Int. J. Greenhouse Gas Control 106, 103282.
- Zhang, K., Jin, Z., Li, \bar{G} ., Liu, Q., Tian, L., 2023. Gas adsorptions of geological carbon storage with enhanced gas recovery. Sep. Purif. Technol. 311, 123260.
- Zhao, W., Zhu, R., Hu, S., Hou, L., Wu, S., 2020. Accumulation contribution differences between lacustrine organic-rich shales and mudstones and their significance in shale oil evaluation. Pet. Explor. Dev. 47 (6), 1160–1171.